ELSEVIER

NeuroImage

www.elsevier.com/locate/ynimg
NeuroImage 32 (2006) 643 – 653

Cerebral perfusion mapping using a robust and efficient method for deconvolution analysis of dynamic contrast-enhanced images

T.S. Koh,[a,b,*] C.K. Markus Tan,[b] L.H. Dennis Cheong,[b] and C.C. Tchoyoson Lim[c]

[a]*Center for Modeling and Control of Complex Systems, School of Electrical and Electronic Engineering, Nanyang Technological University, 50 Nanyang Ave, Singapore 639798, Singapore*
[b]*Center for Signal Processing, School of Electrical and Electronic Engineering, Nanyang Technological University, 50 Nanyang Ave, Singapore 639798, Singapore*
[c]*Department of Neuroradiology, National Neuroscience Institute, 11 Jalan Tan Tock Seng, Singapore 308433, Singapore*

Received 9 March 2006; accepted 23 March 2006
Available online 6 May 2006

Dynamic contrast-enhanced (DCE) imaging using MRI or CT is emerging as a promising tool for diagnostic imaging of cerebral disorders and the monitoring of tumor response to treatment. In this study, we present a robust and efficient deconvolution method based on a linearized model of the impulse residue function, which allows for the mapping of functional cerebral parameters such as cerebral blood flow, volume, mean transit time, and permeability. Monte Carlo simulation studies were performed to study the accuracy and stability of the proposed method, before applying it to clinical study cases of patients with cerebral tumors imaged using DCE CT. Functional parameter maps generated using the proposed method revealed the locations of the cerebral tumors and were found to be of sufficiently good clarity for marked regional differences in tissue vascularity and permeability to be assessed. In particular, tumor visualization and delineation were found to be better on the parameter maps that were indicative of the breakdown of the blood–brain barrier.

Keywords: Cerebral perfusion; Microcirculation; Dynamic contrast-enhanced imaging; Deconvolution

Introduction

Several studies have shown that the ability to assess cerebral perfusion and hemodynamic changes in vivo is potentially useful in the diagnosis and understanding of several pathologies of the brain, such as multiple sclerosis, acute ischemic stroke, and neoplasm (König et al., 2001; Lev et al., 2001; Lüdemann et al., 2001). Dynamic contrast-enhanced (DCE) imaging, using Magnetic Resonance Imaging (MRI) or Computed Tomography (CT), allows for non-invasive, in vivo assessment of physiological parameters associated with cerebral perfusion, such as blood flow, blood volume, mean transit time, and permeability (Østergaard et al., 1998; Nabavi et al., 1999; Sobol and Cure, 2004). DCE MRI or CT is also commonly known as perfusion MRI or perfusion CT in the literature. DCE MRI of cerebral perfusion has been performed using either T_1-weighted (Tofts et al., 1999; Roberts et al., 2001) or T_2-weighted (Østergaard et al., 1996; Calamante et al., 2002) imaging sequences, and the latter is also called dynamic susceptibility contrast-enhanced (DSC) MRI or 'bolus tracking'.

The technique of DCE imaging involves the intravenous injection of a contrast medium and subsequent sequential imaging to simultaneously monitor the concentration of contrast in the tissue of interest $C_{\text{tiss}}(t)$ and a feeding artery $C_{\text{a}}(t)$, as functions of time t. These concentration–time curves are first estimated from the DCE images, to allow for subsequent quantitative assessment of the underlying perfusion parameters. In DCE MRI, as the signal is not in general, linearly related with the contrast medium (gadolinium) concentration, appropriate transformation schemes have been proposed to estimate the concentration–time curves from the DCE images (Østergaard et al., 1996; Calamante et al., 2002). In the case of DCE CT imaging, although the CT number (Hounsfield units) can be linearly related with the iodinated contrast concentration (Lee, 2002), a disadvantage is its use of ionizing radiation. To reduce the radiation dose, lower voltage or current protocols for DCE CT are typically used (Wintermark et al., 2005), such that the effective radiation dose is not much higher than a standard unenhanced CT of the brain (Nabavi et al., 1999; Wintermark et al., 2005).

Adopting the approach of a linear, time-invariant system (Meier and Zierler, 1954; Koh et al., 2003), the relationship between the residual concentration of contrast in the tissue $C_{\text{tiss}}(t)$ and the arterial input $C_{\text{a}}(t)$ can be described as a convolution integral:

$$C_{\text{tiss}}(t) = F\rho \int_0^t C_a(\tau)R(t-\tau)d\tau \quad (1)$$

* Corresponding author. Fax: +65 6792 0415.
E-mail address: etskoh@ntu.edu.sg (T.S. Koh).
Available online on ScienceDirect (www.sciencedirect.com).

1053-8119/$ - see front matter © 2006 Elsevier Inc. All rights reserved.
doi:10.1016/j.neuroimage.2006.03.042

where F is the blood flow or perfusion, and ρ denotes the tissue density (often assumed unity). $R(t)$ is the impulse residue (response) function, which describes the fraction of contrast medium remaining in the tissue as a function of time, due to an unit input impulse of the contrast medium. The product $F{\cdot}R(t)$ contains further information on the other microcirculatory parameters (such as blood volume, transit time and permeability) and can be considered a characteristic function of the underlying tissue and contrast medium used (Meier and Zierler, 1954). Hence, an important objective for the quantitative assessment of cerebral perfusion using DCE imaging is the estimation of $FR(t)$ associated with the underlying tissue of interest, which can be achieved by the process of deconvolution.

We present a robust deconvolution method for the analysis of cerebral DCE imaging data and the estimation of the underlying microcirculatory parameters. Monte Carlo simulation studies were carried out to evaluate the accuracy and consistency of the proposed method and to compare with a more elaborate model-based method. Although the proposed deconvolution method can also be used for DCE MRI data (Østergaard et al., 1996), in this study, we have tested the method on DCE CT images of patients with brain tumors, to illustrate its applicability in actual clinical studies.

Materials and methods

For DCE imaging using MRI or CT, a single-location imaging sequence can be executed to obtain a series of n images with time interval Δt, such that the concentration–time curves, $C_{\text{tiss}}(t)$ and $C_a(t)$, are estimated at $t = t_i = i\Delta t$, where $i = 1, \ldots, n$. A common algebraic approach is hence to discretize the convolution integral equation (Eq. (1)) into a system of linear equations that can be represented in matrix notation as

$$\mathbf{b} = \mathbf{A}\mathbf{x} + \varepsilon, \tag{2}$$

where $\mathbf{x}$ and $\mathbf{b}$ are column vectors with elements given by $x_i = FR(t_i)$ and $b_i = C_{\text{tiss}}(t_i)$, respectively. The error ε is assumed to be additive, and $\mathbf{A}$ is an $n \times n$ matrix whose elements depend on the quadrature rule used to approximate the convolution integral. For example, with a trapezoidal approximation, the elements of $\mathbf{A}$ can be given by

$$a_{ij} = \begin{cases} \frac{\Delta t}{2} \cdot C_a\left(t_{i-j+1}\right) & j = 1, j = i \\ \Delta t \cdot C_a\left(t_{i-j+1}\right) & 1 < j < i \\ 0 & i < j \end{cases},$$

for $i, j = 1, \ldots, n$. Here, deconvolution refers to the process of solving for $\mathbf{x}$ (and hence $F{\cdot}R(t)$), and the problem can be re-cast into one with the minimization of residues, in a least squares sense:

$$\min|\mathbf{A}\mathbf{x} - \mathbf{b}|^2 \tag{3}$$

with n unknowns in $\mathbf{x}$.

Numerical deconvolution in the presence of noise is inherently an ill-posed problem, and the direct matrix inversion of Eq. (2) may not yield useful results. Robust implementations usually attempt to include some form of regularization to achieve stability and to arrive at reasonable solutions. Regularization methods vary according to the deconvolution approach. For example, in the Singular Value Decomposition (SVD) methods, regularization of the SVD solution can be achieved by specifying an appropriate truncation parameter (Østergaard et al., 1996; Koh et al., 2004), and in Fourier transform methods, regularization can be imposed in the form of filters that attenuate certain undesirable frequencies. Another purpose of regularization is to incorporate certain prior knowledge or assumptions about the likely form of the solution into the deconvolution process, so that the final outcome can be more acceptable. For instance, in DCE imaging, we know that the tissue impulse residue function $R(t)$, by its definition, is a positive-definite, non-increasing function (Meier and Zierler, 1954), and such requirements can be imposed on the solution $\mathbf{x}$, in the form of regularization or constraints (Koh et al., 2004).

Rationale for using the distributed parameter R(t) as prior knowledge for deconvolution

Certain prior information on the possible functional behavior of $R(t)$ can be deduced from a tracer kinetics model of tissue microcirculation. Tracer kinetic models for analysis of DCE imaging data are usually linear compartmental models, which can be broadly categorized as conventional compartmental (CC) or distributed parameter (DP) models (Cheong et al., 2004; Tofts et al., 1999). The CC models assume instantaneous diffusion of tracer (i.e., tracer concentration gradients within compartments are assumed zero at all times) while the DP model describes the concentration of tracer as a function of both time and position within the compartments (Larson et al., 1987; Koh et al., 2003). The formulation equations of both CC and DP models are provided in the Appendix to show that the DP model is theoretically more realistic in describing the kinetics of blood flow and exchange in a capillary–tissue unit, as compared to the CC model.

When choosing an appropriate model to describe DCE imaging data, we should also take into consideration the temporal resolution of the data. If the time interval Δt between scans is long, then the diffusion or movement of tracer appears 'instantaneous'. Hence, the compartments could be approximated as 'well-mixed', and the CC models could be used to describe such datasets with long imaging intervals. However, if Δt is appreciably shorter than the typical transit time within the tissue, then one might not be able to justify the use of CC models which assume well-mixed compartments. Instead, for short imaging intervals, one should consider a DP model which does not assume instantaneous tracer movement in the vasculature. With modern CT and MRI technologies, dynamic cerebral imaging can be performed at per second or even subsecond intervals between scans, and since the typical tracer transit time in cerebral tissues range about 3–6 s (Eastwood et al., 2002; Vonken et al., 2000; Østergaard et al., 1998), DP models can be used to appropriately describe such datasets.

An important advantage of the DP model for analysis of cerebral DCE imaging data is that the DP impulse residue functions can display features related to parenchyma processes that reveal certain pathologic conditions of brain tissues (Cheong et al., 2004). As depicted in Fig. 1, the two-compartment DP model of $R(t)$ consists of two physiologic phases:

$$R_{\text{DP}}(t) = R_{\text{v}}(t) + R_{\text{p}}(t), \tag{4a}$$

with

$$R_{\text{v}}(t)(t) = 1 - u(t - t_1) \tag{4b}$$

and

$$R_{\text{p}}(t) = u(t - t_1)\left\{1 - \exp(-k_{21}t_1)\int_0^{t-t_1} y_2(\tau)d\tau\right\} \tag{4c}$$

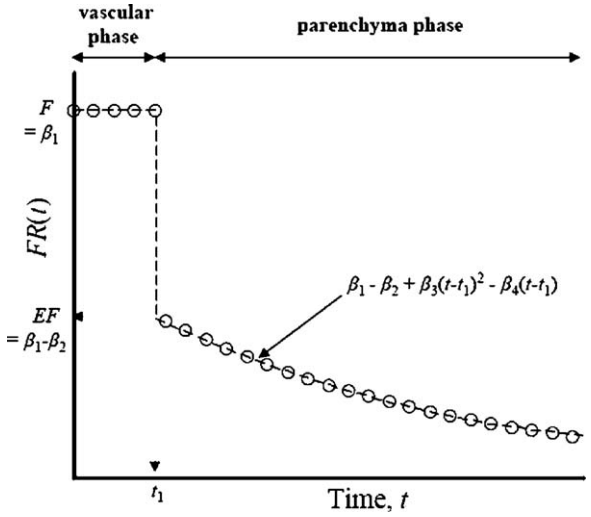

Fig. 1. Schematic diagram of the impulse residue function $FR(t)$ (scaled by blood flow F) of the DP model (circles) and the proposed linearized approximation (dashed line).

representing the vascular and parenchyma phases, respectively. $u(t)$ is the Heaviside unit step function, t_1 denotes the average time needed for the tracer to traverse the vascular compartment, and k_{ij} denotes the rate constant for transfer from compartment j to compartment i (with compartments 1 and 2 respectively representing the vascular and interstitial spaces).

$$y_2(t) = \exp(-k_{12}t)\delta(t) + \exp(-k_{12}t) \times \sqrt{\frac{t_1 k_{21} k_{12}}{t}} I_1\left(2\sqrt{t_1 k_{21} k_{12} t}\right), \quad (5)$$

where I_1 is the modified Bessel function, and $\delta(t)$ is the Dirac delta function.

During the vascular phase, $R_v(t)$ remains constant for a time t_1, reflecting the fact that an external detector registers a constant response proportional to the total amount of tracer in the injected bolus within the region-of-interest, ROI (Larson et al., 1987; Koh et al., 2003). In some pathologic conditions of the brain that result in a compromise of the normally intact blood–brain barrier (BBB) (such as the presence of highly permeable blood vessels in a tumor), a portion of the tracer could diffuse into the extravascular extracellular space. This proportion of tracer that leaks into the extravascular extracellular space can be estimated by the first-pass extraction ratio $E = 1 - \exp(-k_{21}t_1)$ (Larson et al., 1987; Koh et al., 2003). After t_1, the tracer that was not extracted and remains in the intravascular space, exits through outflowing blood, which results in a sudden decrease in $R_{DP}(t)$. The vascular phase is then followed by a parenchyma phase, during which a more gradual decrease in $R_{DP}(t)$ occurs as the extracted portion diffuses back into the intravascular space and is cleared by means of blood outflow.

Since the normal white matter (WM) and grey matter (GM) tissues are associated with an intact BBB, $R_{DP}(t)$ exhibits only the vascular phase, during which $R_{DP}(t)$ remains constant, followed by a rapid decrease to zero, as shown in Fig. 1. This difference in behavior of the DP impulse residue functions between normal cerebral tissues and tumor for DCE CT of patient study cases has been previously reported (Cheong et al., 2004).

Considering that the DP model is theoretically more complete than the CC model (see Appendix), and for DCE images acquired with short time intervals, it would be more appropriate to implement a DP model in the analysis of the DCE images. However, a drawback of the DP model as compared with the CC model is the more elaborate numerical computations involved in the calculation of the DP model (Koh et al., 2003). Hence, it would be of interest to devise an efficient deconvolution approach which could yield similar parameter estimates as the DP model, but with reduced computations.

Physiology-based regularization using a linearized approximation of $R_{DP}(t)$

With the understanding of the possible behavior of $R_{DP}(t)$ as our "prior knowledge", the idea is to adopt the different physiologic shapes of $R_{DP}(t)$ for normal and tumor tissues as the desirable features to be incorporated into the deconvolution problem (Eq. (3)), so as to arrive at solutions which mimic the form of $R_{DP}(t)$.

We first construct a linearized approximation of $R_{DP}(t)$, by defining

$$x_L(t_i) = \begin{cases} \beta_1 & t_i \le T_i \\ \beta_1 - \beta_2 + \beta_3(t_i - t_1)^2 - \beta_4(t_i - t_1) & t_i > t_1 \end{cases} \cong FR_{DP}(t_i) \quad (6)$$

where $\beta_1 = F$, $\beta_2 = F - EF$, and β_3 and β_4 are parameters for a quadratic (time) approximation to the parenchyma phase of $R_{DP}(t)$, as depicted in Fig. 1. We note that although Eq. (6) is quadratic in time, it is, however, linear in the parameters β_1, β_2, β_3, and β_4. Hence, we may denote the linearized approximation of $FR(t)$ in Eq. (6) as a piecewise-continuous, linear (PCL) model. For normal cerebral tissues with an intact BBB, $\beta_2 \to \beta_1$, and β_3, $\beta_4 \to 0$ to give a vanishing parenchyma phase. In matrix notation, Eq. (6) can be represented compactly as

$$\mathbf{x}_L = \begin{bmatrix} 1 & 0 & 0 & 0 \\ 1 & 0 & 0 & 0 \\ \vdots & \vdots & \vdots & \vdots \\ 1 & -1 & (t_k - t_1)^2 & -(t_k - t_1) \\ 1 & -1 & (t_{k+1} - t_1)^2 & -(t_{k+1} - t_1) \\ \vdots & \vdots & \vdots & \vdots \\ 1 & -1 & (t_n - t_1)^2 & -(t_n - t_1) \end{bmatrix} \begin{bmatrix} \beta_1 \\ \beta_2 \\ \beta_3 \\ \beta_4 \end{bmatrix} = \mathbf{X}\beta \quad (7)$$

where t_k is the first time point bigger than t_1.

For the elements x_L to be non-increasing and non-negative, we require $\beta_1, \beta_2, \beta_3, \beta_4 \ge 0$, $\beta_4 = 2(t_n - t_1)\beta_3$, and $X\beta = 0$. These constraints can be formulated linearly as

$$\mathbf{G}\beta = \begin{bmatrix} 1 & 0 & 0 & 0 \\ 0 & 1 & 0 & 0 \\ 0 & 0 & 1 & 0 \\ 0 & 0 & -2(t_2 - t_1) & 1 \\ & & \mathbf{X} & \end{bmatrix} \beta \ge 0. \quad (8)$$

Let $\mathbf{Z} = \mathbf{AX}$, hence, $\mathbf{Ax}_L = Z\beta$, and we see that the present deconvolution problem can be re-cast into the following constrained, linear least squares problem:

$$\min|\mathbf{Z}\beta - \mathbf{b}|^2, \text{ subject to } \mathbf{G}\beta \ge 0. \quad (9)$$

In this way, we have restricted the form of the PCL solution to resemble that of $R_{DP}(t)$ and also reduced the number of unknowns to 5, i.e., β and t_1. For a specified value of t_1, β in Eq. (9) has only 4 unknowns and can be readily solved using a quadratic programming approach (Matlab^{TM}). We may then perform a one-dimensional search for the optimum t_1 that yields the smallest residue in Eq. (9).

The microcirculatory parameters that can be directly estimated using the PCL method are F, t_1, and E. With these parameters, we may further estimate the vascular volume v_1 using the central volume principle, $v_1 = Ft_1$ (Meier and Zierler, 1954); and the permeability-surface product PS, using the Renkin–Crone equation (Renkin, 1959; Crone, 1965):

$$E = 1 - \exp(-PS/F) \tag{10}$$

Monte Carlo simulation experiments

The Monte Carlo simulation approach was used to study the stability of the proposed PCL method, and its ability to yield similar parameter estimates for F, t_1, E, v_1 and PS, as those of the DP model. The simulation experiments were set up in a similar fashion as in (Østergaard et al., 1996). The simulated arterial input curve was in the form of a gamma density function

$$C_a(t) = \begin{cases} C_0(t-t_0)^{\alpha} e^{-(t-t_0)/\beta} & t > t_0 \\ 0 & \text{otherwise} \end{cases}, \tag{11}$$

with $C_0 = 1$, $t_0 = 0$, $\alpha = 3.0$ and $\beta = 1.5$. Using $R_{DP}(t)$ and the simulated $C_a(t)$, the tissue concentration curve $C_{tiss}(t)$ can be simulated using Eq. (1). Three types of $C_{tiss}(t)$ curves were simulated, corresponding to WM, GM, and tumor. The respective DP model parameters assumed for the various tissue types (listed in Table 1) were obtained from a previous study on DCE CT of cerebral tumors (meningiomas) using the DP model (Cheong et al., 2004).

Synthetic dynamic images (Østergaard et al., 1996; Calamante et al., 2002) were constructed using the simulated $C_{tiss}(t)$ curves with each dataset consisting of 50 images of 32 × 32 voxels (i.e., 1024 $C_{tiss}(t)$ curves) and a time interval Δt of 1 s. Gaussian noise was added to the synthetic dynamic images to generate signal-to-noise ratios (SNRs) of 5, 10, and 20, which are typical of DCE imaging (Østergaard et al., 1996). SNR was taken to be the ratio of the maximum value of $C_{tiss}(t)$ (before noise was added) and the standard deviation of noise (Østergaard et al., 1996). Similar to previous works (Østergaard et al., 1996), a preprocessing step of smoothing with a 3 × 3 median kernel was applied to the synthetic images, before performing deconvolution analysis. The proposed PCL deconvolution method was applied to the noisy simulated datasets for WM, GM and tumor. To compare the parameter estimates obtained using the PCL method with those of the actual DP model (Eqs. (4a), (4b) and (4c)), each simulation run was also fitted using the DP model, by the approach of minimizing the residues between simulated data and model (Cheong et al., 2004; Koh et al., 2003).

DCE CT patient studies and image processing

The proposed PCL deconvolution scheme was also applied to DCE CT images of actual patient studies, to illustrate its applicability in the clinical setting. Informed consent was obtained from patients who were recruited in a study to evaluate the feasibility of using DCE CT for assessment of cerebral perfusion in intracranial mass lesions. The protocol for DCE CT was similar to that used in Cheong et al. (2004). Specifically, a slip-ring, helical CT scanner (HiSpeed; GE Medical Systems) that allows for cine mode scanning was used and the dynamic CT images were obtained on a single section at the level of the largest tumor diameter identified on non-contrast CT scans. 50 contrast-enhanced images were acquired with a scanning time of 1 s per image and with the intravenous injection of 50 ml of non-ionic iodinated contrast medium (Omnipaque 300 mgI/ml) at a rate of 4 ml/s using an automatic injector. Parameters for the CT scans were 80 kVp, 190 mAs, 512 by 512 matrix, 20–22 cm field of view and at 10 mm collimations. Accordingly, the slice thickness was 10 mm, and the voxel sizes ranged from 1.53 mm^3 to 1.85 mm^3.

The CT images were transferred to a Pentium IV personal computer for further processing. The images were registered (SPM software package; University College, London, UK) relative to the first image as a template, to correct for any patient movement during the scans. The procedures for sampling of the arterial input $C_a(t)$ and correction for partial volume effects, followed closely those reported in Cheong et al. (2004). We did not attempt to remove recirculation features in both the $C_a(t)$ and $C_{tiss}(t)$ curves, during the calculation of the parameter maps. To account for the different fractional hematocrit associated with $C_{tiss}(t)$ and $C_a(t)$, F can be multiplied by a scaling factor of $(1 - r\text{Hct})/(1 - \text{Hct})$ (Nabavi et al., 1999; Henderson et al., 2003), where Hct is the large vessel hematocrit, and r is the ratio of small to large vessel hematocrit. Following Nabavi et al. (1999), we have used values of 0.4 and 0.8 for Hct and r, respectively.

For each patient study case, parametric maps of F, t_1, E, v_1, and PS were calculated using the PCL method. To generate the parameter maps, the CT numbers within the 4 voxels of each 2-by-2 voxel block were averaged and treated as a single larger voxel. To account for the difference in bolus arrival time between the tissue voxels and the arterial input $C_a(t)$, an additional adjustable parameter t_0 can be included in the expression for $C_{tiss}(t)$ to impose a delay relative to $C_a(t)$, i.e., $C_{tiss}(t - t_0)$, since $C_a(t)$ should be associated with an earlier bolus arrival time than the tissue voxels. Alternatively, one may estimate the difference in bolus arrival times as a separate parameter, before performing deconvolution analysis. This can be achieved by fitting each

Table 1
Values of the various microcirculatory parameters of the DP model used to simulate tissues of normal white matter (WM), normal grey matter (GM) and tumor (meningioma), in the Monte Carlo simulation studies

Tissue types	F (ml/100 g/min)	t_1 (s)	k_{21} (min^{-1})	k_{12} (min^{-1})	v_1 (%)	E	PS (ml/100 g/min)
Tumor	72.43	6.94	5.06	2.66	8.38	0.44	42.0
GM	29.71	3.23	0.20	0.08	1.60	0.01	0.32
WM	19.93	2.95	0.14	0.06	0.98	0.01	0.14

individual concentration–time curve to a delayed gamma density function (Eq. (11)), to estimate the initial rise time (t_0 in Eq. (11)) as the bolus arrival time. In this study, to avoid the additional step of fitting gamma density functions, both t_0 and t_1 were simultaneously adjusted in $C_{tiss}(t - t_0)$ to yield the smallest residue in Eq. (9), when generating the parameter maps. We should also note that although the difference in bolus arrival time between $C_a(t)$ and $C_{tiss}(t)$ is inherent in the DCE images, it is however, not a property or characteristics of the DP model, which describes the tissue microcirculation upon (after) the arrival of the bolus in the tissue.

Results

Monte Carlo simulation experiments

Results of the Monte Carlo simulation studies on the precision of various microcirculatory parameters obtained using the PCL method, are shown in Fig. 2, for SNRs of 5, 10, and 20, and for the various tissue types. For appropriate comparison, the corresponding parameter estimates obtained by data fitting of the DP model are also shown in Fig. 2. For both the PCL method and DP model, the standard deviation of the parameter estimates generally increase somewhat linearly with the decrease of SNR, except for E and PS. Examples of simulated noisy tissue curves for tumor, GM, and WM are shown in Fig. 3, together with the fittings (i.e., vector **b** in Eq. (2)) obtained using the PCL method. The corresponding deconvolved $FR(t)$ functions obtained using the PCL method are also shown together with those of the DP model used to simulate the various tissue types.

Patient study cases

Two representative study cases of different types of cerebral tumors are presented here to illustrate the applicability of proposed PCL method for cerebral perfusion mapping. A 54-year-old patient with metastases from the lungs is shown in Fig. 4. A contrast-enhanced CT image (at $t = 20$ s) is shown together with the various parameter maps generated using the PCL method. The CT image revealed a ring-like lesion with increased contrast medium enhancement on the right frontal lobe of the brain. Correspondingly, the parameter maps for vascular volume v_1 and perfusion F depicted a more vascularized peripheral rim with increased measurements, as compared to the necrotic core, which is associated with markedly lower values of F and v_1.

Fig. 5 shows a contrast-enhanced CT image (at $t = 20$ s), and the parameter maps for a 67-year-old man who was diagnosed with two tumors, a meningioma and a primary pituitary adenoma. The meningioma appears exceptionally 'bright' on the contrast-enhanced CT image, and a corresponding highly perfused region corresponding to the location of the meningioma is also revealed on the v_1 and F maps. Although the extent and boundary of the pituitary tumor is less readily visible on the raw CT images, the E and PS maps clearly revealed the location of the tumor, with increased values.

Discussion

Comparing the Monte Carlo simulation results in Fig. 2, both the PCL method and the DP model generally yielded similar outcomes in terms of accuracy and consistency, under the noise

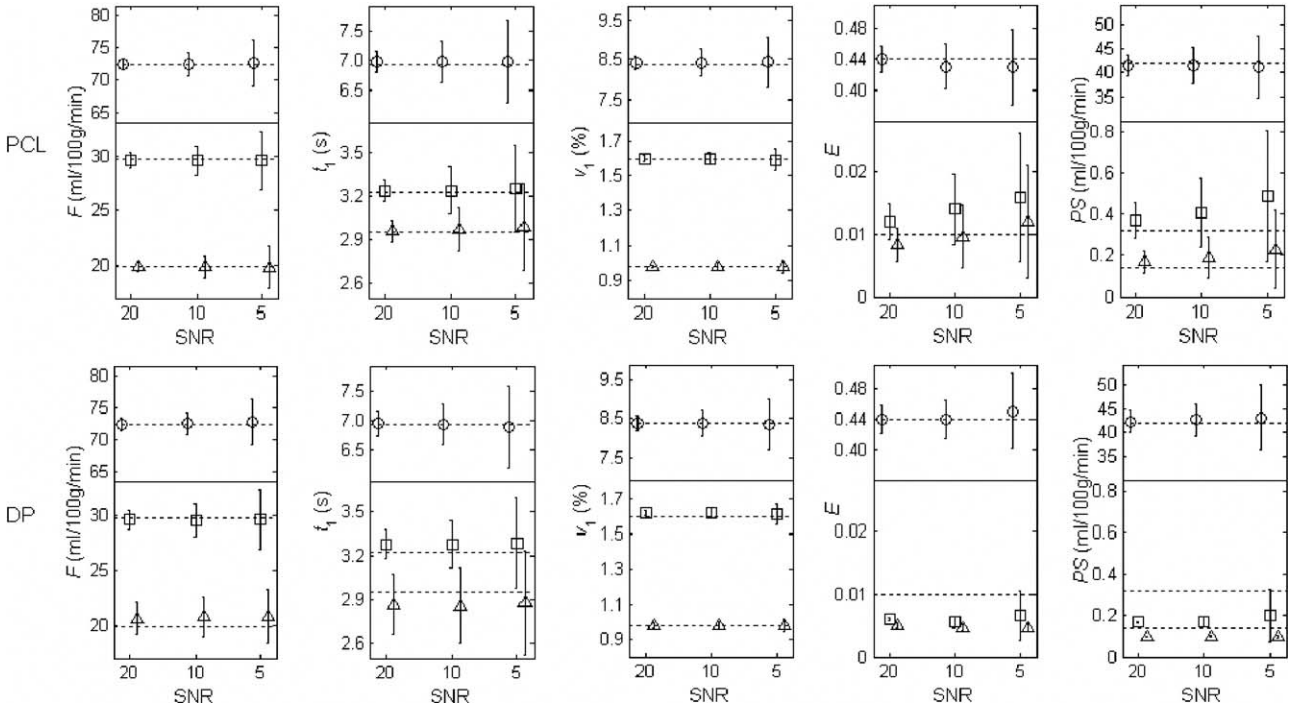

Fig. 2. Results of Monte Carlo simulation studies on the accuracy and consistency of the proposed PCL method (top row) and DP model (bottom row) in estimating the various microcirculatory parameters for tumor (circles), GM (squares), and WM (triangles). The position of each symbol and the associated error bar, respectively, indicate the mean and the standard deviation of 1024 simulation runs. The corresponding dotted lines give the original values used in the simulation (as shown in Table 1).

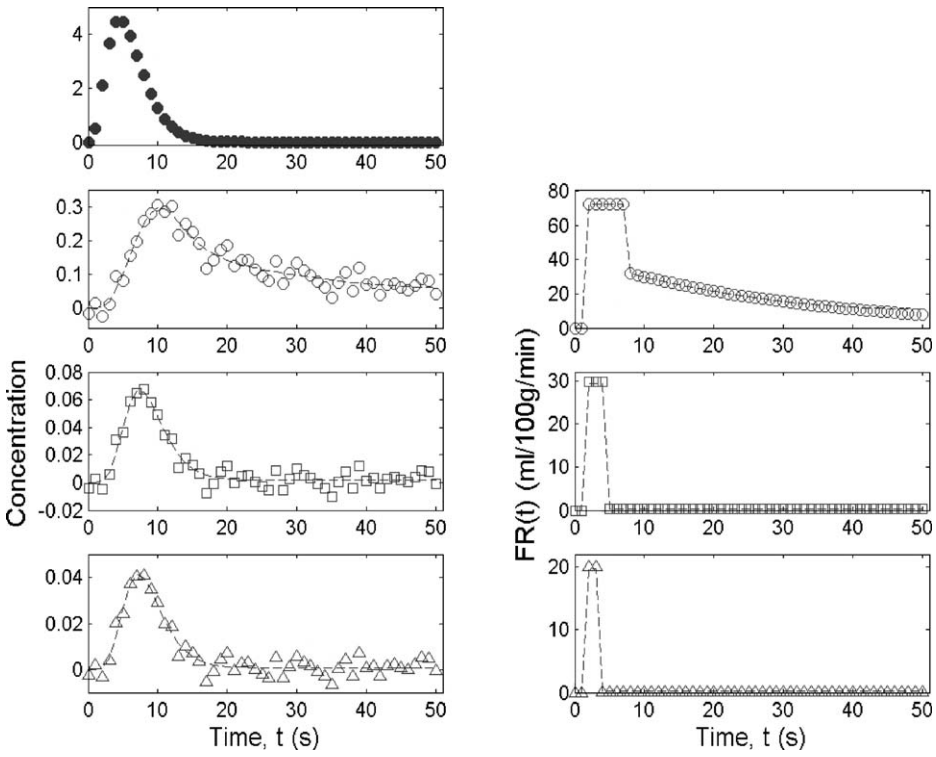

Fig. 3. In the Monte Carlo simulations, the gamma density function used to simulate the arterial input function, is shown here by the filled circles. The following concentration–time plots show examples of noisy simulated $C_{tiss}(t)$ curves for tumor (white circles), GM (squares), and WM (triangles) extracted from the synthetic dynamic images (SNR = 5) after median filter smoothing; and the corresponding dashed lines show the fittings (i.e., vector **b** in Eq. (2)) achieved by the PCL method. In the $FR(t)$ plots, the various symbols denote the original DP models used in the simulation of the noisy $C_{tiss}(t)$ curves, and the dashed lines show the corresponding deconvolved $FR(t)$ functions from the noisy $C_{tiss}(t)$ curves, by the PCL method. A constant t_0 (=1s) was assumed in the simulations.

levels of SNR 5, 10, and 20. For the PCL method, the mean values of the various parameters showed only slight deviations from their respective assumed values in Table 1. The standard deviations of the parameter estimates generally increased with the level of noise and were within about 16% of their assumed values, except for E and PS of the normal WM and GM. Since the assumed values of E and PS of the normal WM and GM were small, slight deviations from these near-zero values would result in large percentage

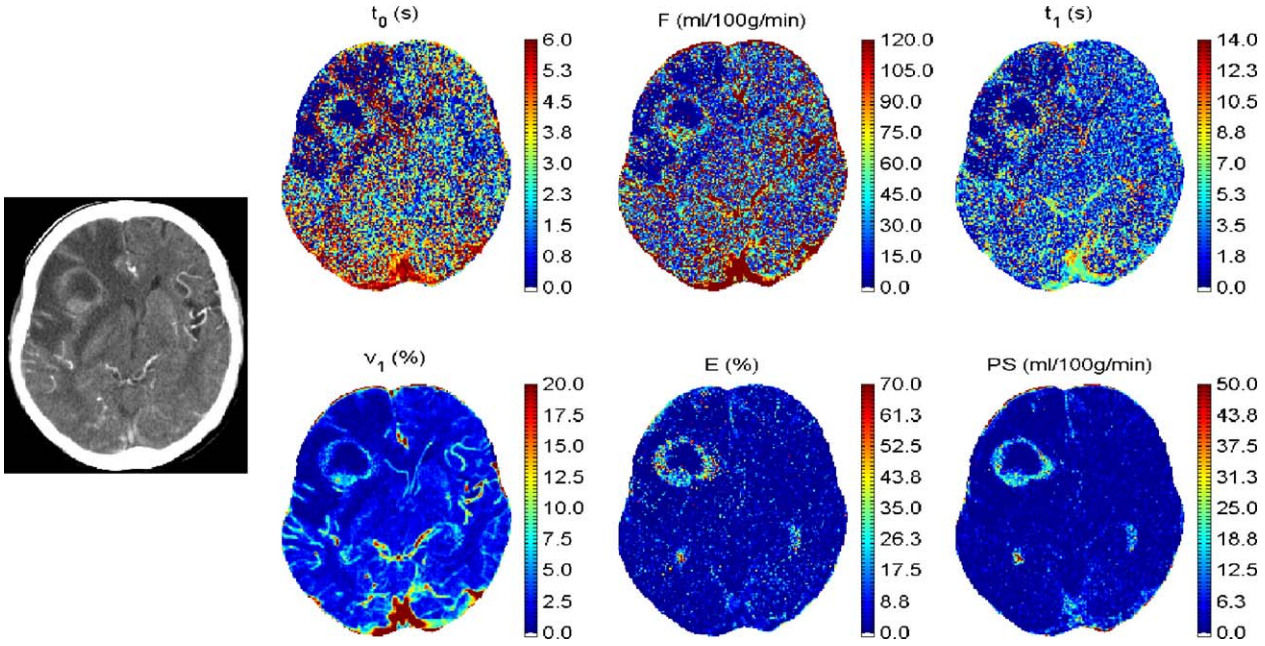

Fig. 4. Case study of a 54-year-old man with a metastatic tumor (from the lungs) on the right frontal lobe of the brain.

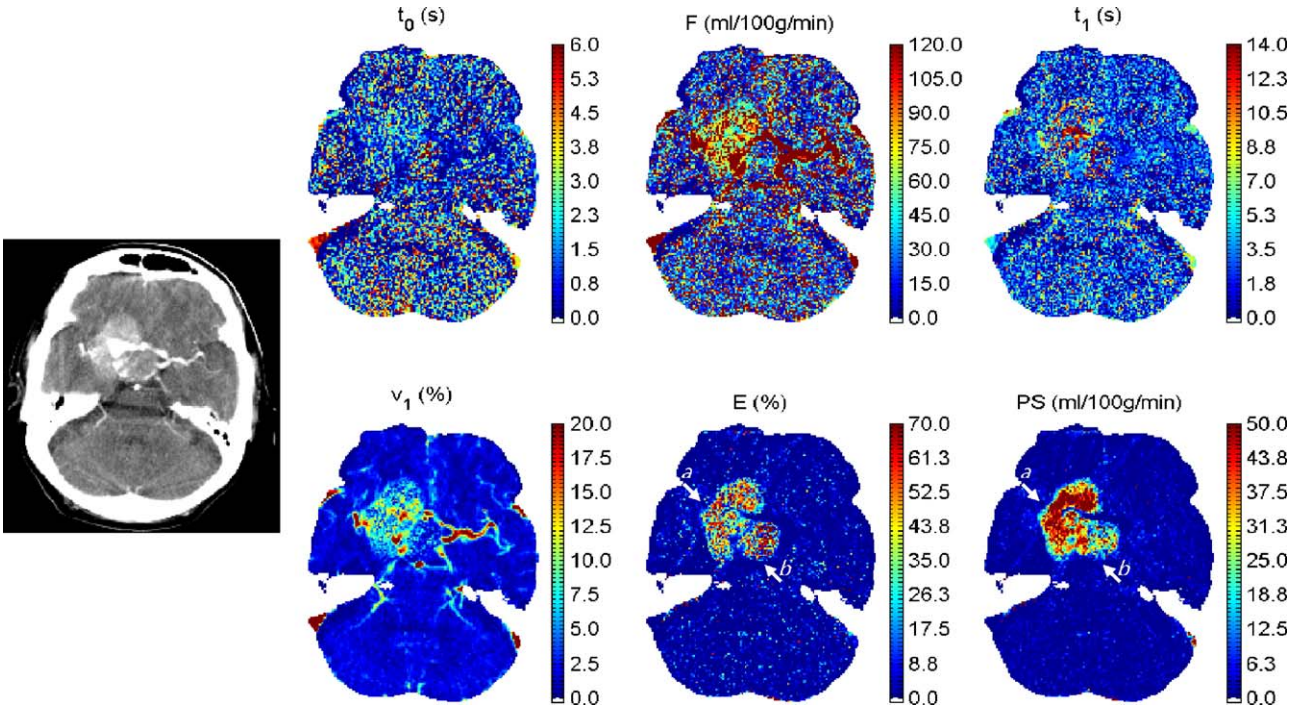

Fig. 5. Case study of a 67-year-old man with a meningioma and pituitary adenoma (indicated by arrows *a* and *b*, respectively, on both the *E* and PS maps) at the base of the skull.

fluctuations. These Monte Carlo simulation results indicate that the proposed PCL method can yield parameter estimates which are consistent with the DP model, and that the PCL method is stable under typical noise conditions of DCE images obtained clinically.

On a Pentium IV personal computer, the PCL method typically takes about 2 min for a set of 1024 simulation runs, while the calculation of the DP model requires about 26 min. For the DP model, the calculation of each $R_{DP}(t)$ requires a numerical integration (Koh et al., 2003) which is rather time consuming, while $x_L(t)$ in the PCL method can be computed based on direct matrix operations (Eq. (7)). Hence, the main advantage of the PCL method as compared with the DP model is its speed of computation (which is about 10 times faster). This improvement in computation speed also facilitated the use of the PCL method in the calculation of functional perfusion maps corresponding to the various microcirculatory parameters, as illustrated in Figs. 4 and 5.

Interestingly, the v_1 and F maps in Fig. 4 not only reveal a necrotic core surrounded by a more viable rim, they also reveal poorly perfused tissues with appreciably lower values of v_1 and F in the edematous tissue immediately surrounding the tumor. The ring-like appearance of the hyperperfused tumor in the E and PS maps implies that the periphery of the tumor contains neoplastic tissues that not only contain a higher vascular fraction and blood flow, but these tissues are also associated with higher leakage (or extravasation) of blood plasma, resulting in the vasogenic edema surrounding the tumor. The demarcation of this peripheral ring of tumor cells is more obvious on the E and PS maps, in contrast with the non-neoplastic tissues that are associated with much lower extravasation values.

Consistently, in Fig. 5, the E and PS maps also demonstrated better demarcation of the tumors, as regions with markedly higher values than the surrounding cerebral tissues. It is interesting to note that the two tumors presented seemingly different perfusion characteristics. The pituitary tumor (arrow b) is associated with lower values of v_1 and F and is less readily visible on the v_1 and F maps, as compared with the meningioma (arrow a), indicating that the primary pituitary tumor is less perfused. On the PS map, the meningioma appears 'hotter' than the primary tumor, even though they have similar E values. This is because PS is related to both E and F according to Eq. (10). In this case, the permeability of the meningioma was markedly higher than those of the primary tumor due to the higher perfusion rate F for the meningioma. This is consistent with the patho-physiological characteristics of the meningiomas, which is known to be more 'leaky' than the primary tumors. In general, these parameter maps generated using the proposed PCL method provided sufficiently good resolution and clarity for the visualization of the various structures in the brain.

However, we note that the present F and t_1 maps could not show good contrast between GM and WM tissues, while the v_1 maps may appear better. We believe this lack of contrast between GM and WM in the F and t_1 maps could be due to a combination of reasons: (a) higher variances in the parameter estimates of F and t_1, as compared to v_1, especially at SNR 5 (as indicated by the Monte Carlo simulation results in Fig. 2), and (b) the averaging of 2×2 voxels as larger voxels which could result in 'smearing' of the difference between the GM and WM signal values (Hounsfield numbers). In our tracer-enhanced CT images, voxels in the larger vessels and tumor are associated with higher SNRs ($\sim$10 or above), since these voxels are more enhanced than those of GM and WM. However, in the GM and WM regions, the SNR for each voxel typically drops to lower than 5, and averaging 2×2 voxels into larger voxels yielded increased SNRs close to 5. Consequently, between adjacent averaged voxels, the distinction between GM and WM parameter values might appear more gradual and hence lacking in contrast. Also, for a challenging SNR of 5, if the actual F and t_1 values are close for the adjacent larger voxels, then the

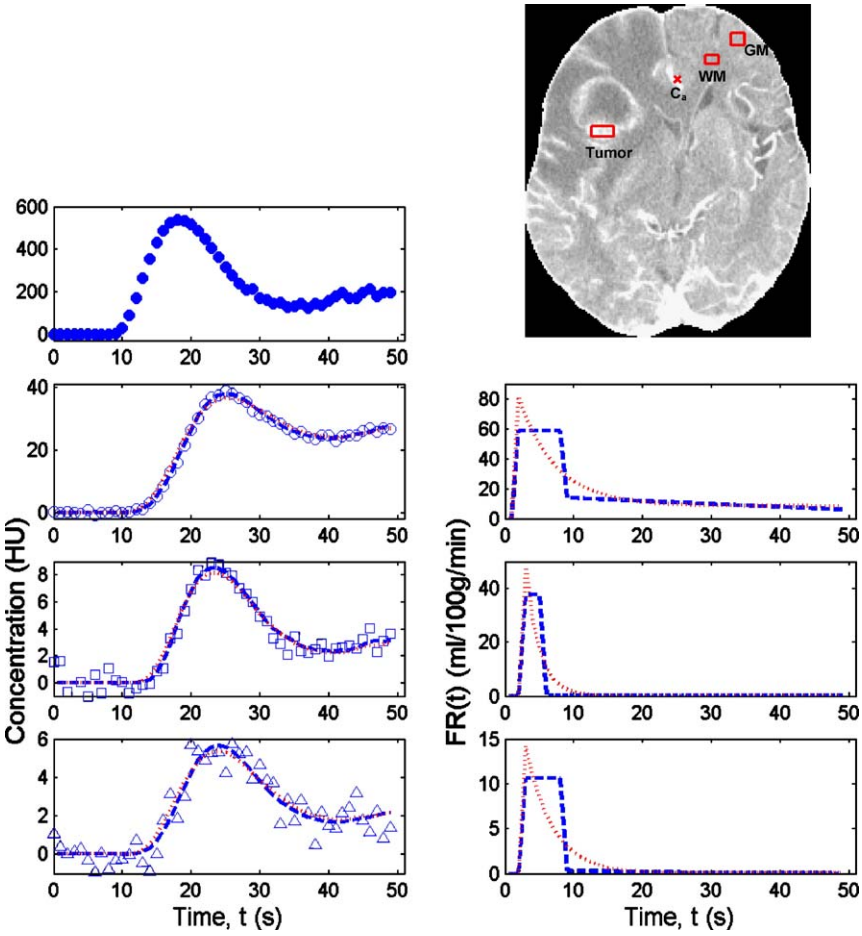

Fig. 6. Results of ROI analysis for the study case shown in Fig. 4. On the brain mask, the rectangular ROIs indicate the locations where the averaged concentrations-time curves for tumor (white circles), GM (squares), and WM (triangles) were sampled; and the cross indicates the location where the arterial input function $C_a(t)$ (filled circles) was sampled. For each concentration–time plot, the dashed and dotted lines show the fittings obtained by the PCL method and the CC model, respectively. The corresponding $FR(t)$ plots show the deconvolved impulse residue functions of the various tissue types, obtained by the PCL method (dashed lines) and CC model (dotted lines).

high estimation errors associated with these parameters could result in overlapping values, giving rise to reduced contrast.

In the t_0 maps of the patient study cases, voxels associated with the veins appear 'hotter' than those of the arteries, since the t_0 parameter give the relative difference in bolus arrival time between the tissue and arterial input $C_a(t)$. Hence, the t_0 map, together with the F and v_1 maps, may be used to infer the locations of arteries and veins. Physiologically, the t_0 parameter might be more significant in certain situations of stroke where the arrival of blood supply to a region of the brain is delayed, and the affected region might appear hotter on the t_0 map.

Validation studies of the functional form of the DP model have been previously carried in dynamic imaging experiments. Larson et al. (1987) compared DP models with conventional (lumped) compartmental (CC) models on experimental data of radiolabeled-water ($H_2{}^{15}O$) uptake and washout in the brains of rhesus monkeys. They showed that the functional form of the DP model more appropriately described their datasets of high temporal resolution (1s interval). Cenic et al. (1999) implemented a unit-step form of the impulse residue function (for normal cerebral tissues) for deconvolution analysis of their dynamic CT datasets (13 studies on 6 New Zealand white rabbits under normal

Table 2
Values of the various parameter estimates obtained using the PCL and CC models, by fitting the concentration–time curves shown in Fig. 6

	F (ml/100 g/min)	v_1 (%)	t_1 (s)	PS (ml/100 g/min)	E	SSR
PCL model						
Tumor	58.85	6.87	7.0	16.0	0.24	17.01
GM	37.55	1.60	2.5	0.2	0.00	18.90
WM	10.55	1.09	6.2	0.3	0.03	25.58
CC model						
Tumor	87.52	8.67	5.9	10.0		61.06
GM	47.10	1.59	2.0	0.4		23.01
WM	14.40	1.18	4.9	0.0		25.96

conditions) and validated their cerebral blood flow measurements with those obtained using the microsphere method. They found a strong correlation between the two sets of measurements (correlation coefficient $r = 0.837$, P value, $P < 0.001$), and the slope of the regression line was very close to unity (0.97 ± 0.03). Nabavi et al. (1999, 2001) again adopted a similar functional form of the DP model for deconvolution analysis to validate the use of dynamic CT for the assessment of stroke. They showed that blood flow and transit time measurements early after the onset of ischemia allow prediction of the size and location of cerebral infarction with good accuracy. Subsequently, a pilot study in patients with acute middle cerebral artery stroke was carried out (Eastwood et al., 2002), and the authors concluded that dynamic CT imaging with deconvolution analysis (using the DP schematic impulse residue function) provided a promising method for evaluation of cerebral hemodynamics in patients with acute stroke. Henderson et al. (2003) performed dynamic CT studies on prostate cancer and analyzed the data using a DP model with adiabatic approximation (St. Lawrence and Lee, 1998). They found that locations of increased blood flow, volume, and permeability were consistent with the results of standard clinical investigations (biopsy, digital rectal exam and trans-rectal ultrasound).

We have also performed an ROI analysis on one of the patient cases, to study the appropriateness of the different functional forms of the impulse residue function assumed by the PCL method (for normal GM and WM tissues with an intact BBB and tumor with BBB disruption), and to compare with the exponential forms of the impulse residue function given by the CC model (with model formulation given in the Appendix). Results of the ROI analysis are shown in Fig. 6. For each tissue type, the concentration–time $C_{\text{tiss}}(t)$ data (in Hounsfield units, HU) were obtained by averaging the voxels within the respective ROI, at each time point. The 'goodness-of-fit' between model and data can be given by the sum of squared residues (SSR), with a better model fitting resulting in a smaller SSR. Quantitative values of the parameter estimates and SSR obtained by fitting of the PCL and CC models are shown in Table 2.

Both the PCL and CC models yielded reasonably good fittings of the various $C_{\text{tiss}}(t)$ curves, as shown by the respective dashed and dotted lines, against the symbols in the concentration–time plots (Fig. 6). The smaller values of SSR achieved by the PCL model (see Table 2) indicated that the PCL model fitted the data better, which is consistent with the findings of Larson et al. (1987). The respective forms of the $FR(t)$ curves obtained by the PCL method are consistent with the description given by the DP model (in Eqs. (4a), (4b) and (4c)), for the various tissues with intact and disrupted BBB. These results are in agreement with the findings of Cheong et al. (2004) who studied the different functional forms of the DP model in cerebral meningiomas. Also, as shown in Fig. 6, due to the strictly decreasing exponential form of the CC model, it yielded higher values of F (Table 2) in order to fit the initial points of the concentration–time curves. The exponential form of the CC model impulse residue function arises as a result of the assumption of instantaneous diffusion (well-mixed compartments) and implies the immediate outflow of a portion of the tracer once the tracer enters the tissue. In Bassingthwaighte and Goresky (1984), the authors have explained that lumped compartmental models, which do not account for axial gradients in tracer concentration, might not provide an accurate description of blood–tissue exchange, and that the inadequacy of such models would become more evident for tracer data obtained with high temporal resolution early in time.

The quantitative values of the parameter estimates derived using the PCL method were consistent with those reported by (Roberts et al., 2002), who have also studied microvascular permeability in human brain tumors using DCE CT. They have generated parameter maps for cerebral blood flow, blood volume, and permeability using the "CT Perfusion 2" software (GE Medical Systems). They reported PS values of >40 ml/100 g/min and >10 ml/100 g/min, respectively, for a patient with cerebral metastases (history of adenocarcinoma of the rectum and pulmonary, with hepatic metastases), and a patient with known cerebral melanoma metastases. Tumor cerebral blood volume was subtly increased and ranged from 5 to 8% (Roberts et al., 2002). The PS values obtained using the PCL method were > ~15 ml/100 g/min for all tumors in Figs. 4 and 5, and blood volume v_1 ranges from about 5 to 12% for the metastatic tumor and meningioma, shown in Figs. 4 and 5, respectively; and v_1 is only slightly increased (~5%) in a few spots within the primary tumor (Fig. 5).

In summary, we developed a linear, least squares method for deconvolution analysis of DCE images, with solutions that mimic the physiologic behavior of the DP impulse residue functions, so as to differentiate between normal and pathologic cerebral tissues. Monte Carlo simulation studies showed that the proposed PCL method can achieve comparable accuracy and consistency as the DP model, at about 10% the computational cost of the DP model. In the clinical study cases with DCE CT, the parameter maps obtained using the PCL method provided both spatial and functional information with sufficient clarity. The cerebral perfusion characteristics depicted by the various parameter maps were consistent with the pathophysiology of the tumors and illustrated the possibility of using such maps for the investigation and diagnosis of cerebral abnormalities.

Appendix A. Conventional compartmental (CC) model

In DCE CT or MRI, the tracer or contrast medium used (i.e., iodinated or DTPA compounds) may diffuse from the blood plasma within the capillaries, into the tissue interstitial (but not into the cells in the tissue). The two-compartment conventional compartment (CC) model comprises of a vascular compartment and an interstitial compartment, denoted here as compartments 1 and 2, respectively, to account for the intravascular space (IVS) and extravascular, extracellular space. A constant flow rate F is assumed to supply the IVS, and assuming well-mixed compartments for the IVS and EES, the tracer kinetics of this bicompartmental tissue system can be described by the following pair of mass-balance equations:

$$v_1 \frac{dC_1(t)}{dt} = -F\rho C_1(t) - K_{21}C_1(t) + K_{12}C_2(t) + F\rho C_a(t) \quad \text{(A.1a)}$$

$$v_2 \frac{dC_2(t)}{dt} = K_{21}C_1(t) + K_{12}C_2(t). \quad \text{(A.1b)}$$

The transfer constants for transcapillary, bidirectional exchange, K_{21} and K_{12}, are related to their corresponding rate constants (k_{21} and k_{12}) by $k_{ij} = K_{ij}/v_j$ (Tofts et al., 1999). Alternatively, for additional reference, Brix et al. (2004, 1999) have formulated a system of equations similar to Eqs. (A.1a) and (A.1b), using purely plasma flow.

The operational equation for analysis of the DCE imaging data using the CC model can be expressed as

$$C_{\text{tiss}}(t) = F\rho C_a(t) \otimes R_{\text{CC}}(t) \tag{A.2a}$$

where $\otimes$ denotes the convolution operator, and $R_{\text{CC}}(t)$ is the impulse residue function for the two-compartment CC model. $R_{\text{CC}}(t)$ takes the biexponential form

$$R_{\text{CC}}(t) = -A\exp(\alpha t) + (1-A)\exp(\beta t), \tag{A.2b}$$

with

$$\begin{pmatrix}\alpha\\ \beta\end{pmatrix} = \frac{1}{2}\left[-\left(k_{21}+k_{12}+\frac{1}{t_1}\right) \pm \sqrt{\left(k_{21}+k_{12}+\frac{1}{t_1}\right)^2 - 4\frac{k_{12}}{t_1}}\right]$$

and $A = \frac{(\alpha + k_{12} + k_{21})}{(\alpha - \beta)}$.

Appendix B. Distributed parameter (DP) model

In contrast to the above CC model, the two-compartment distributed parameter (DP) model does not assume a homogeneous (well-mixed) IVS and defines the tracer concentration within the IVS as a function of both time and position (z) along the length (L) of the capillary space. Hence, the mass-balance equations are formulated for elemental volumes of lengths dz along the capillary (Larson et al., 1987; Koh et al., 2003), as follows:

$$v_1\frac{\partial}{\partial t}C_1(t,z)dz = -F\rho L\frac{\partial}{\partial z}C_1(t,z)dz - K_{21}C_1(t,z)dz + K_{12}C_2(t,z)dz + F\rho L C_a(t)\delta_z(z)dz \tag{A.3a}$$

$$v_2\frac{\partial}{\partial t}C_2(t,z)dz = K_{21}C_1(t,z)dz - K_{12}C_2(t,z)dz \tag{A.3b}$$

where $\delta_z(z)$ is the Dirac delta function, which specifies that the input function $F\rho C_a(t)$ is acting only at the arterial end ($z = 0$) of the capillary. In this form, the DP model accounts for the processes of convective transport and capillary–tissue exchange. For additional reference, Johnson and Wilson (1966) had adopted an alternative formulation, which included the bolus input in the initial and boundary conditions for the solutions of $C_1(t, z)$ and $C_2(t, z)$.

The operational equation for the DP model can be written as

$$C_{\text{tiss}}(t) = F\rho C_a(t) \otimes R_{\text{DP}}(t) \tag{A.4}$$

and the functional form of the DP impulse residue function, $R_{\text{DP}}(t)$, is given by Eqs. (4a), (4b), (4c) and (5), under 'Materials and methods'. $R_{\text{DP}}(t)$ is separable in time domain as two distinct physiologic phases, to describe a intravascular transport phase $R_{\text{v}}(t)$ and a parenchyma exchange phase $R_{\text{p}}(t)$.

Comparing the formulation mass-balance equations of the CC (Eqs. (A.1a) and (A.1b)) and DP (Eqs. (A.3a) and (A.3b)) models, one can see that the DP model incorporates more realism in the description of tracer transport by defining the IVS tracer concentration $C_1(t, z)$ as a function of both time t and position z along the capillary space. In contrast, for the CC model, by assuming instantaneous movement of the tracer in the IVS (i.e., well-mixed), the IVS concentration is spatially homogeneous throughout, and reduces to a function of time t only, i.e., $C_1(t)$. In traditional systems modeling terminology, Eqs. (A.1a) and (A.1b) (for the CC model) is also called a 'lumped' model (whereby certain attributes are lumped or merged), and conversely, Eqs. (A.3a) and (A.3b) is called a 'distributed parameter' model. Other well-known examples of distributed parameter models include the Navier–Stokes equations in fluid mechanics and the Maxwell equations in electromagnetics (Berger et al., 2000).

The difference in the formulation of the CC and DP models yielded different functional forms for their respective impulse residue functions $R(t)$. For the CC model (Eqs. (A.1a) and (A.1b)), the resulting impulse residue function $R_{\text{CC}}(t)$ is the sum of two exponential functions, while the DP impulse residue function $R_{\text{DP}}(t)$ is separable in time domain as two distinct physiologic phases, which describe a intravascular transport phase and a parenchyma exchange phase. The physiologic significance of these phases in cerebral imaging has been explained together with Eqs. (4a), (4b), (4c) and (5). The interested reader could also refer to Larson et al. (1987) for more information. With the above understanding that the formulation of the DP model is more realistic than the CC model, and considering that DCE images are currently acquired with short time intervals, it would be more appropriate to implement a DP model in the analysis of the DCE images. However, a drawback of the DP model as compared with the CC model is the more elaborate numerical computations involved in the computation of the DP model (Koh et al., 2003). Hence, it would be of interest to devise a deconvolution approach which could yield similar parameter estimates as the DP model but with reduced computations.

We should also note that the above CC and DP models represent a hypothetical capillary–tissue exchange unit, which can be used to describe the averaged effect for a capillary bed within a region-of-interest (ROI) on the DCE image. (An ROI could be a voxel or a group of voxels.) Hence, the parameters F, v_1, and t_1 refer to averaged ('central') values of the capillary bed which can be related by the Central Volume Principle (Meier and Zierler, 1954). To more closely model the distribution of blood flow or transit times due to various pathways within a vasculature, Bassingthwaighte and co-workers (Bassingthwaighte and Goresky, 1984; King et al., 1996) have developed multiple-pathway models to account for the heterogeneity of blood flow. The above DP model can be incorporated into a multiple-pathway model, by inserting an individual DP model into each pathway, as shown in Bassingthwaighte and Goresky (1984) to arrive at a realistic whole-organ model. Alternatively, one could attempt to account for heterogeneity of blood flow or transit time within the capillary bed by incorporating a statistical distribution of transit times, as was previously shown for the DP model (Koh et al., 2006). However, these more elaborate flow or transit time heterogeneity models are also computationally intensive. To the best of our knowledge, linearized deconvolution approaches based on such models have not been published yet.

References

Bassingthwaighte, Goresky, 1984. Modeling in the analysis of solute and water exchange in the microvasculature. In: Renkin, E.M., Michel, C.C. (Eds.), Handbook of Physiology, vol. IV. American Physiological Society, Bethesda, MD, pp. 549–626. Sec 2.

Berger, S.A., Goldsmith, W., Lewis, E.R., 2000. Introduction to Bioengineering. Oxford University Press, Oxford, UK.

Brix, G., Bahner, M.L., Hoffmann, U., Horvath, A., Schreiber, W., 1999. Regional blood flow, capillary permeability, and compartmental

volumes: measurement with dynamic CT-initial experience. Radiology 210, 269–276.
Brix, G., Kiessling, F., Lucht, R., Darai, S., Wasser, K., Delorme, S., Griebel, J., 2004. Microcirculation and microvasculature in breast tumors: pharmacokinetic analysis of dynamic MR image series. MRM 52, 420–429.
Calamante, F., Cadian, D., Connelly, A., 2002. Quantification of perfusion using bolus tracking magnetic resonance imaging in stroke: assumptions, limitations and potential implications for clinical use. Stroke 33, 1146–1151.
Cenic, A., Nabavi, D.G., Craen, R., Gelb, A.W., Lee, T.Y., 1999. Dynamic CT measurement of cerebral blood flow: a validation study. AJNR Am. J. Neuroradiol. 20, 63–73.
Cheong, L.H.D., Lim, C.C.T., Koh, T.S., 2004. Dynamic contrast-enhanced CT of intracranial meningioma: comparison of distributed and compartmental tracer kinetic models—Initial results. Radiology 232 (3), 921–930.
Crone, C., 1965. The permeability of brain capillaries to non-electrolytes. Acta Physiol. Scand. 64, 404–417.
Eastwood, J.D., Lev, M.H., Azhari, T., Lee, T.-Y., Barboriak, D.P., Delong, D.M., Fitzek, C., Herzau, M., Wintermark, M., Meuli, R., Brazier, D., Provenzale, J.M., 2002. CT perfusion scanning with deconvolution analysis: pilot study in patients with acute middle cerebral artery stroke. Radiology 222, 227–236.
Henderson, E., Milosevic, M.F., Haider, M.A., Yeung, I.W.T., 2003. Functional CT imaging of prostate cancer. Phys. Med. Biol. 48, 3085–3100.
Johnson, J.A., Wilson, T.A., 1996. A model for capillary exchange. Am. J. Physiol. 210, 1299–1303.
King, R.B., Deussen, A., Raymond, G.M., Bassingthwaighte, J.B., 1996. Modeling blood flow heterogeneity. Ann. Biomed. Eng. 24, 352–372.
Koh, T.S., Cheong, L.H., Hou, Z., Soh, Y.C., 2003. A physiologic model of capillary–tissue exchange for dynamic contrast-enhanced imaging of tumor microcirculation. IEEE Trans. Biomed. Eng. 50, 159–167.
Koh, T.S., Wu, X.Y., Cheong, L.H., Lim, C.C.T., 2004. Assessment of perfusion by dynamic contrast-enhanced imaging using a deconvolution approach based on regression and singular value decomposition. IEEE Trans. Med. Imag. 23, 1532–1542.
Koh, T.S., Cheong, L.H.D., Tan, C.K.M., Lim, C.C.T., 2006. A distributed parameter model of cerebral blood–tissue exchange with account of capillary transit time distribution. NeuroImage 30, 426–435.
König, M., Kraus, M., Theek, C., Klotz, E., Gehlen, W., Heuser, L., 2001. Quantitative assessment of the ischemic brain by means of perfusion related parameters derived from perfusion CT. Stroke 32, 431–437.
Larson, K.B., Markham, J., Raichle, M.E., 1987. Tracer-kinetic models for measuring cerebral blood flow using externally detected radiotracers. J. Cereb. Blood Flow Metab. 7, 443–463.
Lee, T.Y., 2002. Functional CT: physiological models. Trends Biotechnol. 20, S3–S10.
Lev, M.H., Segal, A.Z., Farkas, J., Hossain, S.T., Putman, C., Hunter, G.J., Budzik, R., Harris, G.J., Buonanno, F.S., Ezzeddine, M.A., Chang, Y., Koroshetz, W.J., Gonzalez, G., Schwamm, L.H., 2001. Stroke 32, 2021–2028.
Lüdemann, L., Grieger, W., Wurm, R., Budzisch, M., Hamm, B., Zimmer, C., 2001. Comparison of dynamic contrast-enhanced MRI with WHO tumor grading for gliomas. Eur. Radiol. 11, 1231–1241.
Meier, P., Zierler, K.L., 1954. On the theory of the indicator-dilution method for measurement of blood flow and volume. J. Appl. Physiol. 6, 731–744.
Nabavi, D.G., Cenic, A., Craen, R.A., Gelb, A.W., Bennett, J.D., Kozak, R., Lee, T.Y., 1999. CT assessment of cerebral perfusion: experimental validation and initial clinical experience. Radiology 213, 141–149.
Nabavi, D.G., Cenic, A., Henderson, S., Gelb, A.W., Lee, T.Y., 2001. Perfusion mapping using computed tomography allows accurate prediction of cerebral infarction in experimental brain ischemia. Stroke 32, 175–183.
Østergaard, L., Weisskoff, R.M., Chesler, D.A., Gyldensted, C., Rosen, B.R., 1996. High resolution measurement of cerebral blood flow using intravascular tracer bolus passages: Part I. Mathematical approach and statistical analysis: Part II. Experimental comparison and preliminary results. Magn. Reson. Med. 36, 715–736.
Østergaard, L., Smith, D.F., Vestergaard-Poulsen, P., Hansen, S.B., Gee, A.D., Gjedde, A., Carsten, G., 1998. Absolute cerebral blood flow and blood volume measured by magnetic resonance imaging bolus tracking: comparison with positron emission tomography values. J. Cereb. Blood Flow Metab. 18, 425–432.
Renkin, E.M., 1959. Transport of potassium-42 from blood to tissue in isolated mammalian skeletal muscles. Am. J. Physiol. 197, 1205–1210.
Roberts, H.C., Roberts, T.P.L., Bollen, A.W., Ley, S., Brasch, R.C., Dillion, W.P., 2001. Correlation of microvascular permeability derived from dynamic contrast-enhanced MR imaging with histologic grade and tumor labeling index: a study in human brain tumors. Acad. Radiol. 8, 384–391.
Roberts, H.C., Roberts, T.P.L., Lee, T.-Y., Dillion, W.P., 2002. Dynamic contrast-enhanced computed tomography (CT) for quantitative estimation of microvascular permeability in human brain tumors. Acad. Radiol. 9, S364–S367.
Sobol, W.T., Cure, J.K., 2004. Can in vivo assessment of tissue hemodynamics with dynamic contrast-enhanced CT be used in the diagnosis of tumors and monitoring of cancer therapy outcomes? Radiology 232, 631–632.
St. Lawrence, Lee, 1998. An adiabatic approximation to the tissue homogeneity model for water exchange in the brain: I. Theoretical derivation: II. Experimental validation. J. Cereb. Blood Flow Metab. 18, 1365–1385.
Tofts, P.S., Brix, G., Buckley, D.L., Evelhoch, J.L., Henderson, E., Knopp, M.V., Larsson, H.B.W., Lee, T.-Y., Mayr, N.A., Parker, G.J.M., Port, R.E., Taylor, J., Weisskoff, R.M., 1999. Estimating kinetic parameters from dynamic contrast-enhanced T1-weighted MRI of a diffusible tracer: standardized quantities and symbols. JMRI 10, 223–232.
Vonken, E.P.A., van Osch, M.J.P., Willems, P.W.A., van der Zwan, A., Bakker, C.J.G., Viergever, M.A., Mali, W.P.T.M., 2000. Repeated quantitative perfusion and contrast permeability measurement in the MRI examination of a CNS tumor. Eur. Radiol. 10, 1447–1451.
Wintermark, M., Sesay, M., Barbier, E., Borbely, K., Dillion, W.P., Eastwood, J.D., Glenn, T.C, Grandin, C.B., Pedraza, S., Soustiel, J.-F., Nariai, T., Zaharchuk, G., Caille, J.-M., Dousset, V., Yonas, H., 2005. Comparative overview of brain perfusion imaging techniques. Stroke 36, e83–e99.